OPEN

Correspondence and
requests for materials
should be addressed to
H.Q.X. (hongqi.xu@ftf.
lth.se; hqxu@pku.edu.
cn)

Parity independence of the zero-bias conductance peak in a nanowire based topological superconductor-quantum dot hybrid device

M. T. Deng[1], C. L. Yu[1], G. Y. Huang[1], M. Larsson[1], P. Caroff[1] & H. Q. Xu[1,2]

[1]Division of Solid State Physics, Lund University, Box 118, S-221 00 Lund, Sweden, [2]Key Laboratory for the Physics and Chemistry of Nanodevices and Department of Electronics, Peking University, Beijing 100871, China.

We explore the signatures of Majorana fermions in a nanowire based topological superconductor-quantum dot-topological superconductor hybrid device by charge transport measurements. At zero magnetic field, well-defined Coulomb diamonds and the Kondo effect are observed. Under the application of a finite, sufficiently strong magnetic field, a zero-bias conductance peak structure is observed. It is found that the zero-bias conductance peak is present in many consecutive Coulomb diamonds, irrespective of the even-odd parity of the quasi-particle occupation number in the quantum dot. In addition, we find that the zero-bias conductance peak is in most cases accompanied by two differential conductance peaks, forming a triple-peak structure, and the separation between the two side peaks in bias voltage shows oscillations closely correlated to the background Coulomb conductance oscillations of the device. The observed zero-bias conductance peak and the associated triple-peak structure are in line with Majorana fermion physics in such a hybrid topological system.

The search for Majorana Fermions[1] in solid state systems, especially in s-wave superconductor (SC)-coupled semiconductor nanowires (NWs) with a strong spin-orbit interaction (SOI), is one of paramount research tasks in physics today[2–11]. By exposing an s-wave SC-coupled semiconductor NW with strong SOI to a sufficiently strong and appropriately oriented magnetic field and, thus, driving the system into topological superconductor (TS) phase, zero-energy quasi-particle states, i.e., Majorana Fermions (MFs), are expected to appear in pair at the two ends of the semiconductor NW. Recently, several groups have reported on their observations of the signatures of zero-energy MFs in charge transport measurements of hybrid SC-semiconductor NW devices[12–15]. In these experiments, InSb or InAs semiconductor NWs are used and contacted by an s-wave SC of NbTiN, Nb, or Al. At zero magnetic field, these superconductor contacted NWs show superconductivity at low temperatures due to the proximity effect. Under the application of an external magnetic field, these NWs can be turned to TS NWs and can host zero-energy MF modes at the ends of the NWs, provided that these NWs are of one-dimensional systems or of quasi-one-dimensional systems with an odd number of subbands occupied[11]. In the charge transport measurements, these MF states manifest themselves as a zero-bias conductance peak (ZBCP). The quasi-particles carrying these modes are shown theoretically to obey non-Abelian statistics and could be utilized for topological quantum computing. However, the non-Abelian statistics of Majorana quasi-particles in solid state has not been demonstrated experimentally. It has been suggested that an intriguing experimental demonstration of the non-Abelian statistics is to carry out a braiding experiment of two Majorana quasi-particles in a TS system. In such an experiment, the two MF modes from different MF pairs could be brought to interact via a non-topological object. It is, therefore, fundamentally important to study the novel physics of TS systems in the presence of such interaction.

Several other physical mechanisms could also lead to a ZBCP in the charge transport measurements of the experimentally studied SC-semiconductor NW hybrid systems, such as the Kondo effect, the Josephson super-current, Andreev reflections, level crossing, quantum phase transition, transport through impurity states, and the effects of disorder in potential and magnetic field distributions. The most of these effects can be conclusively excluded from the reported experiments[12,13,15]. However, the question regarding whether the Kondo correlation

could be a physical mechanism for the observed ZBCPs in these experiments or some of these experiments is still in active debate[16] and requires a conclusive experimental study.

Here, we report on the realization and measurements of a hybrid Nb-InSb NW-Nb quantum device, in which a normal InSb quantum dot (QD) is present between two superconductor Nb-contacted InSb NW segments. Under an sufficiently strong magnetic field applied perpendicularly to the substrate (and thus to the NW) and a suitable back-gate voltage, the two Nb-contacted InSb NW segments could turn to become two TS NWs and each could host a pair of Majorana fermion modes at its ends. Electrical measurements between the two Nb-contacted InSb NW segments in the trivial superconductor phase and in the TS phases are employed to detect possible appearance of the Majorana fermion modes and to study the effect of the interaction between the two Majorana modes located adjacent to the InSb QD. To block the contribution of the supercurrent, we tune the QD to the Coulomb blockade regime. When a sufficiently strong, perpendicular magnetic field is applied to the device, we observe a ZBCP in several consecutive Coulomb blockade diamonds of the QD with both odd and even quasi-particle occupation numbers. Our experiment conclusively rules out the possibility to assign the Kondo physics as a mechanism to the observed ZBCP.

The structure of our Nb-InSb NW QD-Nb hybrid device is schematically shown in figure 1a. The device is fabricated from the zinc-blende InSb part of an epitaxially grown, high crystalline quality, InSb/InAs heterostructure NW[17] on an n-type Si substrate covered by a thin SiO_2 layer on top and a Ti/Au back gate electrode on the bottom side (see Supplementary Information for more details). Two Nb-based superconductor contacts with a separation of 150 nm are defined on the cleaned surface of the InSb NW by electron-beam lithography and an InSb QD is naturally formed at low temperatures between the contacts at appropriate voltages applied to the back gate[18,19]. Figure 1b shows a scanning electron microscope (SEM) image of the fabricated device. All the electrical measurements reported in this work are performed in a dilution refrigerator at base temperature $T = 25$ mK.

The measurements of the fabricated device is first performed for the differential conductance at $B = 0$ T as a function of the back gate voltage V_{bg} and the source-drain bias voltage V_{sd} (the charge stability diagram). The results of the measurements are presented on a color scale over a large V_{sd} range in figure 1c with a zoom-in plot shown in figure 1d. Here, clear Coulomb blockade diamond structures can be seen, indicating the formation of the QD between the two superconductor contacts[18,19]. Through the Coulomb blockade diamond
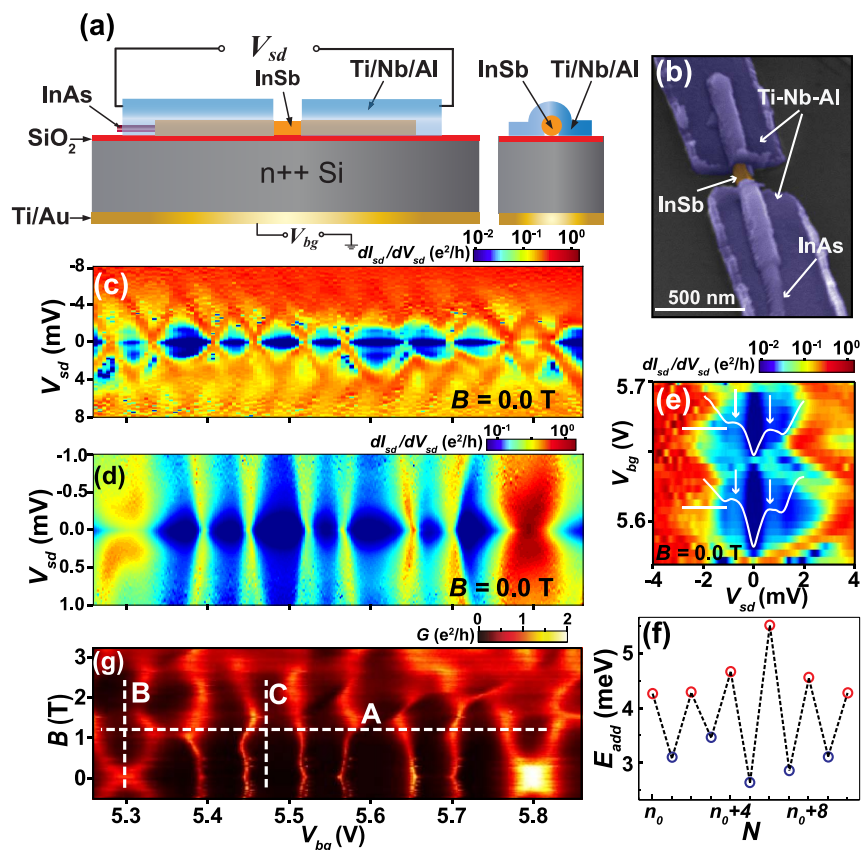

Figure 1 | (a) Schematics showing a side view (left panel) and a cross-section view (right panel) of the structure of a NW based Nb-InSb QD-Nb junction device studied in this work. (b) SEM image of the fabricated Nb-InSb QD-Nb junction device. In this device, the diameter of the InSb NW is about 70 nm, the separation between the two Nb-based contacts is about 150 nm, and the lengths of the InSb NW segments covered by Nb-based contacts are about 780 nm and 720 nm, respectively. (c) Differential conductance on a color scale measured for the device as a function of V_{sd} and V_{bg} (charge stability diagram) at $B = 0$ T. (d) Close-up plot of (c) at the low bias voltage region with a higher bias voltage resolution. (e) Zoom-in view of two Coulomb blockade diamonds in the charge stability diagram measurements shown in (c). The two solid curves show the differential conductance plots (line-cuts) at the fixed gate voltages indicated by two short horizontal lines (i.e., the electron-hole symmetry points of the two Coulomb blockade regions). (f) Addition energy, E_{add}, of a single quasi-particle to the QD extracted from the measurements in (c) as a function of quasi-particle numbers in the QD. Here, a clear even-odd oscillation behavior of the addition energy can be seen. (g) Linear response conductance on a color scale measured for the device as a function of V_{bg} and the magnetic field B. Here, the magnetic field is applied perpendicularly to the substrate and thus to the InSb NW.

structures, two horizontal high conductance stripes separated by a low conductance gap appear in the small V_{sd} region. This conductance feature is seen more clearly in figure 1e, where a zoom-in view of a region of two Coulomb blockade diamonds is displayed together with two line-cut plots.

The high conductance stripes can be attributed to the proximity effect induced superconductivity in the Nb-contacted InSb NW segments with a superconductor energy gap Δ^*. At $V_{sd} = \pm 2e\Delta^*$, the quasi-particle tunneling is enhanced by the alignment of the upper (lower) gap edge of the quasi-particle density of states in one Nb-contacted InSb NW segment with the lower (upper) gap edge of the quasi-particle density of states in the other Nb-contacted InSb NW segment. Therefore, $\Delta^* \sim 0.3$ meV at $B = 0$ T can be deduced from the measurements[13]. The quasi-particle addition energy E_{add} to the QD at $B = 0$ T can also be extracted from the measurements and the results are plotted in figure 1f. It is seen that E_{add} is in the range of 2.7–5.6 meV, which is much larger than Δ^*. E_{add} also shows regular oscillations with increasing quasi-particle number in the QD and, thus, the device shows consecutive alternations in the parity of the quasi-particle occupation number in the QD. Figure 1g shows the linear response conductance on a color scale measured for the device as a function of V_{bg} and magnetic field B applied perpendicularly to the substrate and thus to the InSb NW at $V_{sd} = 4$ μV. The conductance peaks (the bright lines) arise from resonance tunneling through the quasi-particle states in the QD. Due to magnetic-field induced energy shifts of these quasi-particle states, these peaks shift in position of V_{bg} as the magnetic field increases. From the low magnetic field region of the measurements, we can also identify the parity of the quasi-particle number in the QD[18,19]. The results are consistent with the parity extracted from the addition-energy measurements shown in figure 1f.

In both figures 1d and 1g, two high zero-bias conductance stripes, located in the Coulomb blockade regions at back gate voltages around $V_{bg} = 5.3$ V and $V_{bg} = 5.8$ V, can be identified at $B = 0$ T. These conductance enhancements can be attributed to the spin-1/2 Kondo effect in the device with odd quasi-particle occupation numbers in the QD. Note that in a Coulomb blockade region without a clear Kondo effect enhancement, the signatures of Josephson current[20–26], i.e., sharp and high conductance peaks at zero-bias voltage, are not found in this device. This is because the Josephson effect is strongly suppressed in the system in the presence of the Coulomb blockade effect.

To drive the Nb-contacted InSb NW segments of the device from trivial superconducting phase to nontrivial TS phase, application of an external magnetic field B, perpendicular to the Rashba SOI-induced field B_{SO}, is needed. The magnetic field introduces a Zeeman energy $E_z = \frac{1}{2}|g^*|\mu_B \tilde{B}$, where $\mu_B = e\hbar/2m_e$ is the Bohr magneton, g^* is the effective g-factor, and $\tilde{B}$ is the magnetic field actually applied on the Nb-contacted InSb NW segments, which can be greatly different from B due to the Meissner effect. In general, it is difficult to accurately determine the strength of the externally applied magnetic field B_T at which the phase transition in the Nb-contacted InSb NW segments occurs. For our device, according to the measured properties of the Nb thin film (see Supplementary Information), the lower limit value of B_T is estimated to be in the range of $0.33 \sim 0.78$ T.

Figure 2a shows the charge stability diagram with the differential conductance on a logarithmic color scale measured for the device at $B = 1.2$ T, i.e., along dashed line A in figure 1g. Figures 2b and 2c are the corresponding line-cut plots of the differential conductance on the linear scale at small source-drain bias voltages. For clarity and to overcome the influence of the background conductance oscillations due to the Coulomb blockade effect, these line-cut plots are offset in such a way that the values of the differential conductance at $V_{sd} = 0$ μV in these line-cuts are successively placed 0.005 e^2/h higher than

the values of their adjacent, lower gate-voltage line cuts, while their actual zero-bias conductance values are represented by their gray-scale colors. Here, Coulomb diamond structures remain to be clearly seen in the charge stability diagram plot of figure 2a, indicating the survival of the QD in the device in the presence of the 1.2 T magnetic field. In the line-cut plots of figures 2b and 2c, we can see a global conductance gap structure in the small source-drain bias voltage region of $V_{sd} \sim -0.35$ mV to $V_{sd} \sim 0.35$ mV, showing that the Nb-contacted InSb NW segments are still in a superconducting state with an energy gap $\Delta^* \sim 0.17$ meV. Strikingly, a pronounced conductance peak appears at zero-bias voltage and goes through the whole V_{bg} region shown in figure 2, including both the Coulomb blockade regions and quantum resonance regions (see figure 3 in Supplementary Information for three-dimensional views of the measurements). This zero-bias conductance peak (ZBCP) feature is seen in figure 2a and is even more clearly seen in figures 2b and 2c. The ZBCP has a height of up to ~ 0.2 e^2/h at the quantum resonances and of up to ~ 0.06 e^2/h at the electron-hole symmetry points (i.e., at the centers of the Coulomb blockade diamonds). Moreover, the appearance of the ZBCP is independent of the even-odd parity of the quasi-particle occupation number in the QD, i.e., the ZBCP appears in all the Coulomb blockade diamonds shown in figure 2, irrespective of whether even or odd the quasi-particle occupation number in the QD is.

Figure 3 shows the magnetic field dependent measurements of the differential conductance of the device. Figures 3a and 3b display the differential conductance on a logarithmic color scale measured for the device as a function of V_{sd} and magnetic field B perpendicularly applied to the substrate at $V_{bg} = 5.29$ V and $V_{bg} = 5.48$ V, i.e., along dashed lines B and C in figure 1g, respectively. The corresponding line-cut plots of the differential conductance are shown in the linear scale in figures 3c and 3d. Again, for clarity, these line-cut curves are offset in the same way as in figure 2b and 2c with their actual zero-bias conductance values represented by their gray-scale colors.

The magnetic field dependent measurements of the differential conductance shown in figures 3a and 3c are performed in the Coulomb blockade region of an odd quasi-particle occupation number in the QD, while the measurements shown in figures 3b and 3d are performed in the Coulomb blockade region of an even quasi-particle occupation number in the QD (see figures 1g). Again, from these figures, we can see a Δ^*-induced low-conductance gap and a tendency of decreasing in the width of the gap as B increases. Within the Coulomb blockade regions of both the odd and the even occupation number of quasi-particles in the QD, there is no ZBCP structure when the applied magnetic field is small. However, as the applied magnetic field is increased over a certain value, a ZBCP structure emerges in both Coulomb blockade regions. This ZBCP structure is seen to persist in a finite range of magnetic fields before it finally disappears at higher magnetic fields–it emerges at $B \sim 0.6$ T and disappears at $B \sim 1.8$ T in figures 3a and 3c, while in figures 3b and 3d it emerges at $B \sim 0.75$ T and disappears at $B \sim 2.1$ T.

Similar results as in figures 2 and 3 have also been observed in the charge transport measurements of a different NW based Nb-InSb QD-Nb hybrid device (see Supplementary Information). With the presence of several Coulomb blockade diamonds in the charge stability diagram measurements of the devices, we have showed for the first time that the ZBCP structure is independent of the even-odd parity of quasi-particle occupation numbers in the QD. This parity independence would not favor the assignment of the ZBCP structure to the Kondo physics. A possible scenario could be proposed by assignment of these ZBCPs to the MF physics. At a sufficiently strong applied magnetic field and a suitable gate voltage, it is possible to drive the two Nb-covered InSb NW segments in such a device to TS phase, leaving the intermediate QD to remain as a trivial object. Hence, two pairs of MF bound states, spatially separated by the QD, can be created in the TS-QD-TS hybrid system. However, in
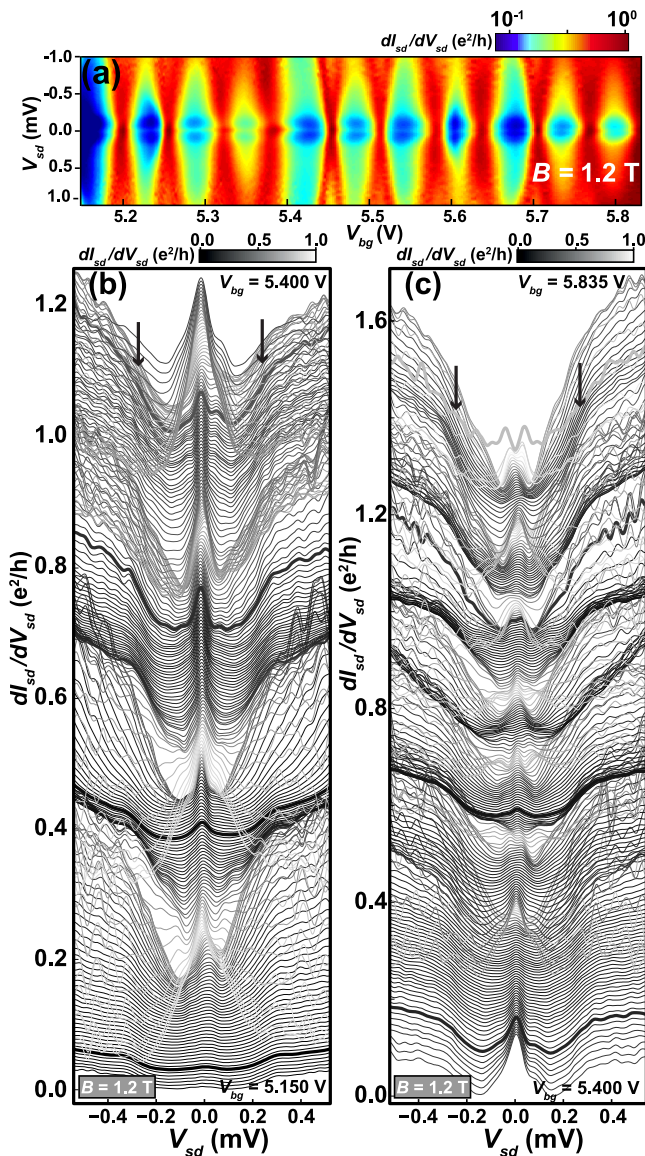
Figure 2 | (a) Charge stability diagram measured for the device at $B = 1.2$ T, i.e., along the dashed line A in figure 1g. It is seen that a stripe of the ZBCP structure appears in every Coulomb blockade diamond found in the figure, irrespective of the quasi-particle occupation number parity in the QD. (b) and (c) Corresponding differential conductance line-cut plots of the measurements at a series of values of V_{bg}. The plots shown in panel (b) are the differential conductance measurements at V_{bg} ranging from 5.15 V to 5.4 V, while the plots shown in panel (c) are that at V_{bg} ranging from 5.4 V to 5.835 V. For clarity, these line-cut plots are shifted in such a way that values of the differential conductance at $V_{sd} = 0$ μV in these line cuts are successively placed 0.005 e^2/h higher than the values of their adjacent, lower gate-voltage line cuts, while their actual zero-bias conductance values are represented by their gray-scale colors. Here, in (b) and (c), the existence of a ZBCP structure in every Coulomb blockade diamond is more clearly displayed. An overall low differential conductance gap (with its two edges indicated by two arrows on top of each panel) in the low bias voltage region due to the presence of the proximity effect induced InSb superconducting energy gap and its weak dependence on V_{bg} can also be identified in (b) and (c). In addition, a few line cuts are highlighted by thicker lines in (b) and (c) in order to help the reader to see the characteristic features in the plots.
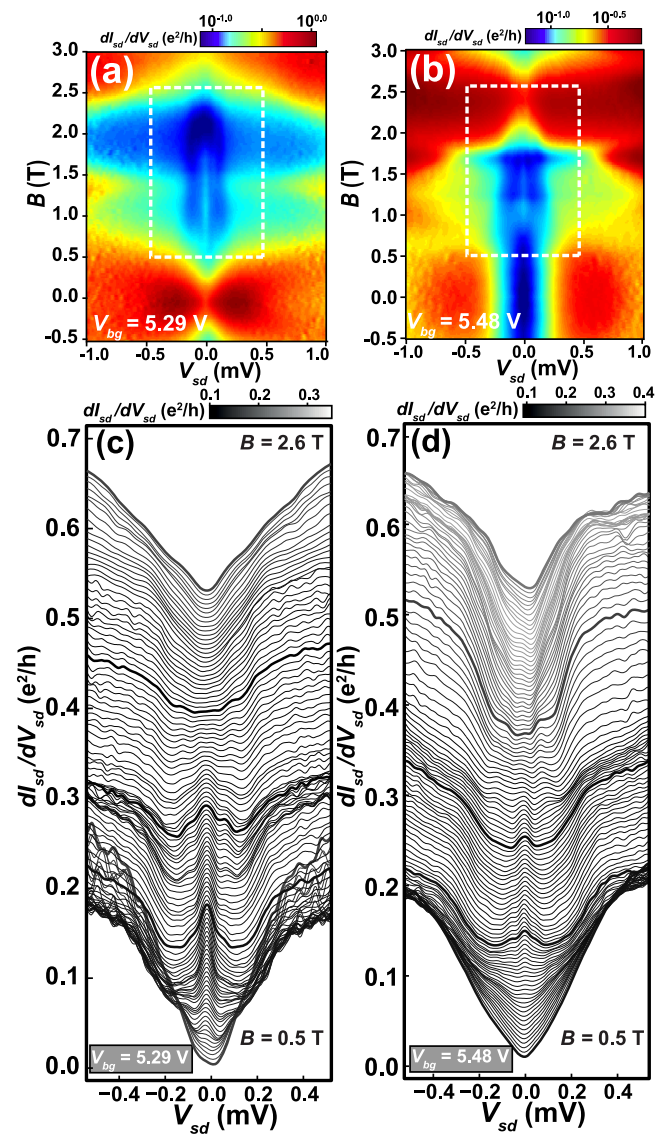
Figure 3 | (a) Differential conductance as a function of the source-drain bias voltage V_{sd} and the perpendicularly applied magnetic field B measured for the device at $V_{bg} = 5.29$ V, i.e., along the dashed line B in figure 1g. (b) The same as (a) but measured for the device at $V_{bg} = 5.48$ V, i.e., along the dashed line C in figure 1g. (c) Line-cut plots of the differential conductance measurements in the bias voltage and magnetic field region indicated by the white dashed rectangle in (a). (d) Line-cut plots of differential conductance measurements in the bias voltage and magnetic field region indicated by the white dashed rectangle in (b). For clarity, these line-cuts are shifted in the same way as in figures 2b and 2c, i.e., in such a way that values of the differential conductance at $V_{sd} = 0$ μV in these line cuts are placed successively 0.005 e^2/h higher than the values of their adjacent, lower magnetic field line cuts, while their actual zero-bias conductance values are represented by their gray-scale colors. The ZBCP in panels (a) and (c) is seen to emerge at $B \sim 0.6$ T and disappear at $B \sim 1.8$ T, while the ZBCP in panels (b) and (d) is seen to emerge at $B \sim 0.75$ T and disappear $B \sim 2.1$ T. Panels (c) and (d) also show an overall low differential conductance gap in the low bias voltage region due to the presence of the proximity effect induced InSb superconducting energy gap and its evolution with increasing magnetic field. A few line cuts are highlighted by thicker lines in (b) and (c) in order to help the reader to identify the characteristic features in the plots.
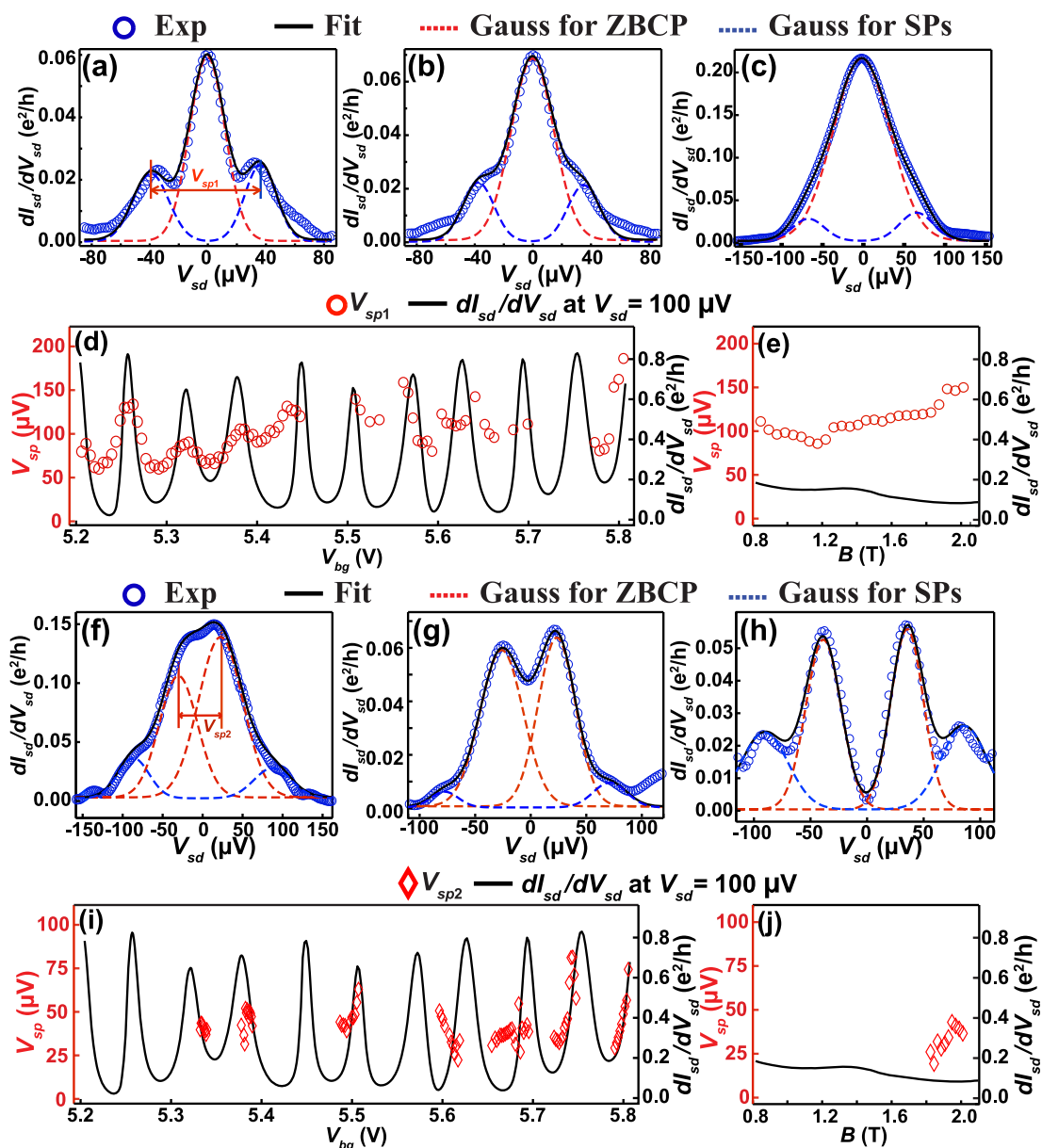
Figure 4 | (a)–(c) Differential conductance as a function of V_{sd} measured at $B = 1.2$ T for the device at $V_{bg} = 5.385$ V, 5.395 V, and 5.445 V, respectively. Blue circles are the experimental data, red dashed lines are the Gaussian fits to the ZBCPs, blue dashed lines are the Gaussian fits to the side peaks, and black solid lines are the overall fitting results to the experimental data obtained by the sum of the Gaussian fits to the ZBCP and to the side peaks. (d) Separation (red circles) of the two side peaks V_{sp1}, as defined in panel (a), extracted from figures 2b and 2c as a function of V_{bg}. The solid line in the panel shows the differential conductance dI_{sd}/dV_{sd} measured for the device at $V_{sd} = 100$ μV. Here, it is seen that the V_{sp1} oscillations and the differential conductance oscillations are closely correlated. (e) Value of V_{sp1} (red circles) extracted from figure 3c as a function of B plotted together with the differential conductance (solid line) measured for the device at $V_{sd} = 100$ μV. (f)–(h) Differential conductance as a function of V_{sd} measured at $B = 1.2$ T for the device at $V_{bg} = 5.765$ V, 5.815 V and 5.835 V, respectively. Here the ZBCP is seen to split into two peaks. Again, blue circles are the experimental data and blue dashed lines are the Gaussian fits to the side peaks. But red dashed lines are the Gaussian fits to the split peaks from the ZBCP. Black solid lines are the overall fitting results to the experimental data obtained by the sum of the Gaussian fits to the peaks split from the ZBCP and to the side peaks. (i) Splitting of the ZBCP V_{sp2} (red circles), as defined in panel (f), extracted from figures 2b and 2c as a function of V_{bg} and the differential conductance (solid line) measured for the device at $V_{sd} = 100$ μV. (j) Value of V_{sp2} (red circles) extracted from figure 3c as a function of B together with the differential conductance (solid line) measured for the device at $V_{sd} = 100$ μV.

the presence of a finite coupling between the two TS NW segments, the two MF bound states located adjacent to the QD (i.e., the inner two MF bound states) can interact and hybridize into a pair of quasi-particle states with finite energies. The other pair of MF bound states (i.e., the outer two MF bound states) located at the two ends of the entire InSb NW remain at zero energy and thus the entire system, including the two Nb-contacted NW segments and the QD, would behave as a nontrivial TS NW (see the Supplementary Information in

Ref. 13). In our experiment, it would be this outer pair of MF states that could make Cooper pair transport between the two Nb contacts possible, leading to an enhancement of the conductance at zero-bias voltage. Because the existence of MF bound states in the TS-QD-TS system is independent of the parity of the quasi-particle occupation number as well as the energy position of the quasi-particle states in the QD, the ZBCP can appear in more than ten consecutive Coulomb blockade diamonds, regardless of the parity of quasi-particle

occupation numbers and the energy position of the quasi-particle states in the QD.

There are several other possible mechanisms that can lead to a ZBCP in a Josephson QD junction, such as the Kondo effect[16], quantum phase transition (QPT)[27], Josephson supercurrent[28,29], Andreev reflections[27], level crossing[18], bound states at impurities[30], and the effects of disorder in potential and magnetic field distributions[31]. The Kondo effect depends strongly on whether the ground state of the QD is spin-singlet or spin-doublet and thereby depends on the parity of the quasi-particle occupation number in the QD, in clear contrast to the observed parity independence of the ZBCP in our experiment. In addition, the Kondo effect (including exotic Kondo effects[32-34]) induced ZBCP will split into two conductance peaks located at finite bias voltages in finite magnetic fields, which is especially true for the InSb NW QD with a giant g^*-factor[18]. However, the observed ZBCP in our system stays at the zero bias voltage for a magnetic field range of >1 T (corresponding to a Zeeman energy of $V_Z \sim 2$ to 4 meV in the InSb NW QD) (figures 3). Hence, it is not consistent to attribute the ZBCP observed in our experiment to the Kondo effect. A magnetic field induced QPT from a singlet to a spin-polarized ground state or from a spin-polarized to a singlet ground state in the QD could also lead to a ZBCP[27]. However, such a QPT is sensitively dependent on the energy position of the quasi-particle state in the QD and spin-resolved Andreev levels and, thus, can only occurs at certain values of V_{bg} and B. Our experiment shows that the observed ZBCP appears continuously over a large range of V_{bg} (covering several Coulomb blockade diamond regions) and a large range of B (>1 T, see the discussion above), which does not resemble the characteristic behavior of the ZBCP derived from the QPT. In order to rule out the possibilities to associate the Josephson supercurrent to the observed ZBCP, we have in the experiment tuned the QD into well-defined Coulomb blockade regions. For a trivial superconductor system, the Cooper pair transport through the QD in such a Coulomb blockade region can be suppressed and no supercurrent induced conductance peak could be observed. However, in strong contrast, our measurements presented in figure 2 show that there exist a ZBCP in several entire Coulomb blockade diamond regions. Thus, the ZBCP feature existing in the entire gate voltage region shown in figure 2 could not be attributed to the supercurrent mechanism (see also figures 4 and 7 in Supplementary Information and the corresponding discussions). The other effects, including Andreev reflections, level crossing, bound states at impurities, and disorder in potential and magnetic field distributions, have already been discussed and excluded from the previously reported experiments[12-15]. These effects are in general sensitive to the magnetic field and the gate voltage, and could only give characteristic ZBCPs at certain values of these experimental tuning parameters[18,27,30,31]. In contrast, the results presented in figures 2 and 3 show that the ZBCPs observed in our experiment are insensitive to the tunings of the magnetic field and the gate voltage, i.e., they constantly appear over a large range of the magnetic field and the gate voltage. Thus, it would not be consistent to attribute the observed ZBCPs in our experiment to these effects.

As we discussed previously, two coherently connected MFs will hybridize into a pair of quasi-particle states with finite energies (see also the Supporting Information in Ref. 13). This hybridization will lead to splitting of the ZBCP and can serve as an important signature of the Majorana physics. In our TS-QD-TS system, there would exist two pairs of zero-energy MFs when there were no coupling between the two TS NW segments. In reality, the two inner MFs can be coherently coupled through the QD, leading to the creation of a pair of quasi-particle states at finite energies, while the outer two MFs can remain intact and staying at zero energy. As a consequence, the transport measurements can show a triple conductance peak structure, with two side differential conductance peaks appearing at finite bias voltages tunable by tuning the quasi-particle states in the QD

and with the middle peak still staying at the zero bias voltage irrespective of the energy positions of the quasi-particle states in the QD.

This triple conductance peak structure has indeed been observed in the measurements shown in figures 2 and 3. Figures 4a–4c show the results of the measurements (open circles) at three selected back-gate voltages of $V_{bg} = 5.385$, 5.395, and 5.765 V, displaying the characteristics of the triple conductance peak structure. In each of these figures, the red dashed line and the two blue dashed lines are the Gaussian fits to the ZBCP and the two side conductance peaks, while the solid black line represents the actual result of the fitting, i.e., the sum of the three individual Gaussian fits. It can be seen in figures 4a–4c that, in all the three cases, the experimental data are well reproduced by the fits.

It is clear that the bias voltage positions of the two side conductance peaks are V_{bg}-dependent. To investigate the behavior of the two side conductance peaks quantitatively, we define V_{sp1} as the distance in V_{sd} between the two side peaks (see the definition in figure 4a) and plot V_{sp1} extracted from figures 2b and 2c as a function of V_{bg} in figure 4d (red circles). It is seen that V_{sp1} shows regular oscillations with amplitudes in a range of 50–150 μV. The black solid line in figure 4d shows the differential conductance measured at $V_{sd} = 100$ μV as a function of V_{bg}, displaying the regular Coulomb conductance oscillations. Evidently, the V_{sp1} oscillations are closely correlated to the Coulomb conductance oscillations in the transport through the QD.

This oscillation correlation phenomenon is consistent with our hypothesis that the hybridization of the two inner MFs are strongly influenced by the quasi-particle states in the QD. When the energy of a quasi-particle state in the QD is aligned with the MF states in the TS NWs, the interaction between the two inner MFs is enhanced via the quasi-particle state, leading to a large separation between the two quasi-particle states and thus a large value of V_{sp1}. However, as the quasi-particle state in the QD is moved away in energy from the MF states in the TS NWs as at the electron-hole symmetry point of a Coulomb blockade diamond region, the interaction between the two inner MFs is reduced and thus a small value of V_{sp1} is observed.

Figure 4e shows V_{sp1} extracted from the measurements presented in figure 3c as a function of the magnetic field and the corresponding differential conductance measured at $V_{sd} = 100$ μV. Here, we see that V_{sp1} shows smooth variation with increasing magnetic field, in contrast to the clear oscillations of V_{sp1} with increasing V_{bg} seen in figure 4d. This is because the device remains in a deep Coulomb blockade region in the whole magnetic field range in figure 4e and there is no on-off resonance alternation induced modulation on the interaction between the two inner MFs.

Finally, it is worthwhile to note that small splittings of the ZBCP have also been observed in the measurements of our device shown in figures 2 and 3 at certain back gate voltages and magnetic fields. Figures 4f–4h show the results of the measurements (open circles) at $V_{bg} = 5.765$, 5.815, and 5.835 V. Here, it is clearly seen that the ZBCP splits into two peaks which, together with the two side differential conductance peaks, form a quadruple conductance peak structure. The quadruple conductance peak structure can also be well fitted by Gaussians as shown by the dashed lines in figures 4f–4h. Similarly as for V_{sp1}, we can define V_{sp2} as the distance in V_{sd} between the peaks split from the ZBCP. Figure 4i shows the value of V_{sp2} (red circles) extracted from the measurements presented in figures 2b and 2c as a function of V_{bg}. However, in contrast to V_{sp1}, V_{sp2} does not show clear correlated oscillations with Coulomb conductance oscillations (the black solid line in figure 4i). It is also observed that the splitting of the ZBCP does not occur at all the resonances and it does not only occur at the resonances either. In particular, the splitting of the ZBCP is seen to occur even in deep Coulomb blockade regions. Figure 4j shows V_{sp2} extracted from the measurements presented in figure 3c as a function of magnetic field and the corresponding differential conductance measured at $V_{sd} = 100$ μV. Here, the splitting

of the ZBCP is clearly seen in the high magnetic field region. However, the ZBCP does not show any visible splitting at any magnetic fields in the magnetic field dependent measurements shown in figure 3d.

Splitting of the ZBCP has recently been predicted as an evidence for the existence of the Majorana modes in a TS NW[35–37]. Based on this prediction, we can attribute the splitting of the ZBCP observed in our experiment to hybridization of the two outer MFs. Similarly as for the two inner MFs in our system, the interaction between the outer two MFs is, in principle, influenced by the chemical potential, Zeeman energy and the quasi-particle states in the QD. However, in comparison with the two inner MFs, the interaction between the two outer MFs is extremely weak and the splitting of the ZBCP is thus much smaller as it is seen in figures 4i–4j.

In summary, we have studied a Nb-InSb NW QD-Nb hybrid device made from an epitaxially grown InSb NW with strong SOI on a Si/SiO$_2$ substrate by charge transport measurements. At zero magnetic field, the device shows a series of well defined Coulomb blockade diamonds and the Kondo effect. At a fixed but sufficiently strong magnetic field applied perpendicularly to the substrate and thus to the NW, a pronounced ZBCP structure is observed in the Coulomb blockade regions and is found to be present in more than ten consecutive Coulomb blockade diamonds, irrespective of the even-odd parity of the quasi-particle occupation number and of the energy position of the quasi-particle states in the QD. We have also observed that the ZBCP is in most cases accompanied by two side differential conductance peaks located at finite bias voltages, forming a triple conductance peak structure. The splitting of the two side peaks is found to be correlated to the background conductance of the device. These observations are consistent with the signatures of MF physics in the device: In a NW based TS-QD-TS system, the two inner MFs are coherently coupled via the QD and are hybridized into a pair of quasi-particles with finite energies, while the two outer MFs remain as zero-energy modes and the entire system behaves as a TS NW.

Methods

Single crystalline, twin-free, zincblende InSb nanowires used in the device fabrication were grown on top of InAs nanowire stems. These axial heterostructure nanowires were grown by metal-organic vapour phase epitaxy on InAs(111)B substrates, decorated by pure gold seed particles, at 450°C. All the grown InSb nanowires were free of any extended structural defects and did not show tapering. The grown axial InAs/InSb heterostructure nanowires were transferred to a 100-nm-thick SiO$_2$ layer capped, degenerately doped, n-type Si substrate with predefined Ti/Au bonding pads and markers. Using an optical microscope, the positions of the wires relative to the metal markers were recorded. Then, two 470-nm-wide Nb-based superconductor contacts with a separation of 100–150 nm were defined on the InSb segment of each selected InAs/InSb heterostructure nanowire using electron beam lithography, sputtering and lift-off techniques. The Nb-based superconducting contacts were of a Ti/Nb/Al (3 nm/80 nm/5 nm) trilayer structure. The 3-nm-thick Ti bottom layer served as an adhesion layer, whereas the top 5-nm-thick Al layer was used for protecting Nb from oxidation. Prior to metal deposition, oxygen plasma treatment was performed in order to remove resist residues. To remove the native oxide layers on the InSb nanowires, we also performed wet etching/passivation in a (NH$_4$)$_2$S$_x$ solution for 60 seconds. The diameters of the etched nanowires were roughly 15 nm smaller than the diameters of these nanowires before etching. In the fabricated device, there was also a Ti/Au metal layer on the back side of the substrate which was employed as a global back gate.

1. Majorana, E. Teoria simmetrica dell'elettronee del positrone. *Nuovo Cimento* **5**, 171–184 (1937).
2. Wilczek, F. Majorana returns. *Nat. Phys.* **5**, 614–618 (2009).
3. Franz, M. Race for Majorana fermions. *Physics* **3**, 24 (2010).
4. Service, R. F. Search for Majorana fermions nearing success at last? *Science* **332**, 193–195 (2011).
5. Alicea, J. New directions in the pursuit of Majorana fermions in solid state systems. *Rep. Prog. Phys.* **75**, 076501 (2012).
6. Nayak, C., Simon, S. H., Stern, A., Freedman, M. & Das Sarma, S. Non-Abelian anyons and topological quantum computation. *Rev. Mod. Phys.* **80**, 1083–1159 (2008).
7. Read, N. & Green, D. Paired states of Fermions in two dimensions with breaking of parity and time-reversal symmetries and the fractional quantum Hall effect. *Phys. Rev. B* **61**, 10267–10297 (2000).
8. Fu, L. & Kane, C. Superconducting proximity effect and Majorana fermions at the surface of a topological insulator. *Phys. Rev. Lett.* **100**, 096407 (2008).
9. Lutchyn, R. M., Sau, J. & Das Sarma, S. Majorana fermions and a topological phase transition in semiconductor-superconductor heterostructures. *Phys. Rev. Lett.* **105**, 077001 (2010).
10. Oreg, Y., Refael, G. & von Oppen, F. Helical liquids and Majorana bound states in quantum wires. *Phys. Rev. Lett.* **105**, 177002 (2010).
11. Stanescu, T., Lutchyn, R. M. & Das Sarma, S. Majorana fermions in semiconductor nanowires. *Phys. Rev. B* **84**, 144522 (2011).
12. Mourik, V. *et al.* Signatures of Majorana fermions in hybrid superconductor-semiconductor nanowire devices. *Science* **336**, 1003–1007 (2012).
13. Deng, M. T. *et al.* Anomalous zero bias conductance peak in a Nb-InSb NW-Nb hybrid device. *Nano Lett.* **12**, 6414–6419 (2012); arXiv:2012.4130.
14. Das, A. *et al.* Zero-bias peaks and splitting in an Al-InAs nanowire topological superconductor as a signature of Majorana Fermions. *Nat. Phy.* **8**, 887–895 (2012).
15. Churchill, H. O. H. *et al.* Superconductor-nanowire devices from tunneling to the multichannel regime: zero-bias oscillations and magnetoconductance crossover. *Phys. Rev. B* **87**, 241401 (2013).
16. Lee, E. J. *et al.* Zero-bias anomaly in a nanowire quantum dot coupled to superconductors. *Phys. Rev. lett.* **109**, 186802 (2012).
17. Caroff, P. *et al.* High-quality InAs/InSb nanowire heterostructures grown by metal-organic vapor-phase epitaxy. *Small* **4**, 878–882 (2008).
18. Nilsson, H. A. *et al.* Giant, level-dependent g factors in InSb nanowire quantum dots. *Nano Lett.* **9**, 3151–3156 (2009).
19. Nilsson, H. A. *et al.* Correlation-Induced Conductance Suppression at Level Degeneracy in a quantum dot. *Phys. Rev. Lett.* **104**, 186804 (2010).
20. Doh, Y.-J. *et al.* Tunable supercurrent through semiconductor nanowires. *Science* **309**, 272–275 (2005).
21. Jørgensen, H. I., Grove-Rasmussen, K., Novotný, T., Flensberg, K. & Lindelof, P. E. Electron transport in single-wall carbon nanotube weak links in the Fabry-Perot regime. *Phys. Rev. Lett.* **96**, 207003 (2006).
22. Xiang, J., Vidan, A., Tinkham, M., Westervelt, R. M. & Lieber, C. M. Ge/Si nanowire mesoscopic Josephson junctions. *Nat. Nanotechnol.* **1**, 208–213 (2006).
23. Nilsson, H. A., Samuelsson, P., Caroff, P. & Xu, H. Q. Supercurrent and multiple Andreev reflections in an InSb nanowire Josephson junction. *Nano Lett.* **12**, 228–233 (2012).
24. Abay, S. *et al.* High critical-current superconductor-InAs nanowire-superconductor junctions. *Nano Lett.* **12**, 5622–5625 (2012).
25. Abay, S. *et al.* Quantized conductance and its correlation to the supercurrent in a nanowire connected to superconductors. *Nano Lett.* **13**, 3614–3617 (2013).
26. Abay, S. *et al.* Charge transport in InAs nanowire Josephson junctions. *Phys. Rev. B* **89**, 214508 (2014).
27. Lee, E. J. *et al.* Spin-resolved Andreev levels and parity crossings in hybrid superconductor-semiconductor nanostructures. *Nat. Nanotechnol.* **9**, 79–84 (2013).
28. van Dam, J. A., Nazarov, Y. V., Bakkers, E. P. A. M., De Franceschi, S. & Kouwenhoven, L. P. Supercurrent reversal in quantum dots. *Nature* **442**, 667–670 (2006).
29. Deon, F. *et al.* Proximity effect in a two-dimensional electron gas probed with a lateral quantum dot. *Phys. Rev. B* **84**, 100506 (2011).
30. Sau, J. D. & Demler, E. Bound states at impurities as a probe of topological superconductivity in nanowires. *Phys. Rev. B* **88**, 205402 (2013).
31. Adagideli, I., Wimmer, M. & Teker, A. Effects of electron scattering on the topological properties of nanowires: Majorana fermions from disorder and superlattices. *Phys. Rev. B* **89**, 144506 (2014).
32. Schmid, J., Weis, J., Eberl, K. & v. Klitzing, K. Absence of odd-even parity behavior for Kondo resonances in quantum dots. *Phys. Rev. Lett.* **84**, 5824 (2000).
33. Sasaki, S. *et al.* Kondo effect in an integer-spin quantum dot. *Nature* **405**, 764–767 (2000).
34. Jarillo-Herrero, P. *et al.* Orbital Kondo effect in carbon nanotubes. *Nature* **434**, 484–488 (2005).
35. Das Sarma, S., Sau, J. D. & Stanescu, T. D. Splitting of the zero bias conductance peak as smoking gun evidence for the existence of the Majorana mode in a SC-SN NW. *Phys. Rev. B* **86**, 220506 (2012).
36. Rainis, D., Trifunovic, D., Klinovaja, J. & Loss, D. Towards a realistic transport modeling in a super-conducting nanowire with Majorana fermions. *Phys. Rev. B* **87**, 024515 (2013)
37. Cheng, M., Becker, M., Bauer, B. & Lutchyn, R. M. Interplay between Kondo and Majorana interactions in quantum dots. arXiv:1308.4156.

Acknowledgments

Author contributions

M.T.D. and C.L.Y. fabricated the devices and performed the measurements and data analysis. G.Y.H. carried out the theoretical modeling and participated in the experimental

data analysis. M.L. assisted with the measurements and participated in the experimental data analysis. P.C. performed the MOVPE growth of the nanowires and participated in the discussion of the results. H.Q.X. conceived and directed the project, performed the data analysis, and participated in the construction of the theoretical model. M.T.D. and H.Q.X. wrote the manuscript. All authors reviewed the manuscript.

Additional information